J Therm Anal Calorim (2012) 109:1493–1502
DOI 10.1007/s10973-011-1916-8

An investigation into sintering of PA6 nanocomposite powders for rotational molding

Antonio Greco · Alfonso Maffezzoli · Emanuela Calò · Claudia Massaro · Roberto Terzi

Received: 4 May 2011 / Accepted: 12 September 2011 / Published online: 28 September 2011

Abstract The objective of this work is to study the sintering behavior of polyamide 6 (PA6) powders and PA6 nanocomposites by means of thermomechanical (TMA) and dimensionless analysis in view of its technological application in rotational molding. TMA analysis was used to monitor the bulk density evolution of PA6 powders and PA6 nanocomposites when heated above the melting temperature. Experimental TMA results indicate that the sintering of PA6 and PA6 nanocomposites occurs in two different steps, namely powder coalescence and void removal. Furthermore, TMA analysis showed that relevant degradation phenomena occur during the sintering of PA6 and PA6 nanocomposites, leading to gas formation in the molten polymer. The suitability of these materials in rotational molding was then assessed by defining a processing window, as the temperature difference between the endset sintering and the onset degradation. The heating rate dependence of the processing window was explained by means of dimensionless analysis, showing that powder coalescence is influenced by the viscosity evolution of the matrix, whereas void removal is influenced by the gas diffusivity inside the molten matrix. Therefore, the diffusion activation energy correlates the endset sintering temperature to the heating rate. On the other hand, the onset degradation temperature depends on the heating rate, due to the characteristic activation energy of the degradation process. Accordingly, the width of the processing window mainly depends on the values of the activation energies for diffusivity and degradation. The width of the processing window for neat PA6 was found to be too narrow to candidate this polymer for rotational molding. The addition of nanofiller causes a narrowing of the processing window, whereas the PA6 matrix modified with a thermal stabilizer showed a sufficiently broad processing window, compatible for use in rotational molding.

Keywords Nanocomposites · Polyamide 6 · Sintering · Thermomechanical analysis (TMA)

A. Greco (✉) · A. Maffezzoli
Department of Engineering for Innovation, University of Salento, Via per Monteroni, 73100 Lecce, Italy
e-mail: antonio.greco@unisalento.it

E. Calò · C. Massaro · R. Terzi
Advanced Physical Technologies and New Materials Department, ENEA—Italian National Agency for New Technologies, Energy and the Environment, S.S. 7—Km 714, 72100 Brindisi, Italy

Introduction

Sintering of semi-crystalline polymers occurs in those industrial processes, such as rotational molding, where the material is heated in the absence of any external applied pressure [1, 2]. Sintering of polymers, defined as the formation of a homogeneous melt from particles [2], is a double stage mechanism, involving powder coalescence [1–3] and void removal [4]. Surface tension forces drive coalescence, while viscous forces must be overcome to obtain full powder coalescence [3]. Therefore, solid state sintering is not possible for polymers, whereas the coalescence of particles begins only when certain conditions of molecular mobility are achieved, i.e., above the glass transition temperature for amorphous polymers and in the molten state for semicrystalline polymers [2]. A high viscosity of the polymer melt can be responsible for a high fraction of voids [4] and consequently of a poor quality of parts.

The sintering behavior of commodity polymer has been widely studied, with particular attention to processes such

as rotational molding, in which the final quality of molded parts is significantly influenced by the sintering behavior of powders [3–10].

On the other hand, in recent years, significant attention has been devoted to the sintering behavior of high performance, engineering thermoplastics, such as polyamides, polyesters, aromatic polychetones, polycarbonate, and their nanocomposites, with a particular attention toward selective laser sintering, a rapid prototyping process [11–17]. Furthermore, in recent years different types of polyamides have been developed to meet the increasing demands of rotomolding industry of high performance products. Among these, polyamide 11 (PA11) and polyamide 12 (PA12) are attracting a growing interest in several industrial applications [18]. Nevertheless, such materials are very expensive and their mechanical and thermal properties are much lower than those of polyamide 6 (PA6). Although, PA6 compounds for rotational molding have been used, the high melting temperature and the low thermo-oxidative stability of PA6 require the use of a non-oxidative atmosphere during rotomolding. In literature, most of the studies that deal with the sintering of engineering thermoplastics try only to establish a correlation between the process parameters and the final quality of the products in terms of mechanical and physical properties. The mechanisms involved in the sintering of engineering thermoplastic have not been investigated yet. Another new aspect is given by the modification of the sintering characteristic of a polymer deriving from the addition of a nanofiller.

On the other hand, it has been shown that thermomechanical analysis (TMA) is suitable for studying the sintering behavior of ceramic [19] and polymeric [5, 6, 20] powders. TMA allows on-line monitoring of the sample bulk density as a function of temperature, and therefore it is suitable to study the kinetics of sintering, giving useful information on the mechanisms involved in powders coalescence and void removal.

The objective of this study is to analyze the sintering behavior of PA6 powders and PA6 nanocomposites by TMA, in view of a potential application in rotational molding. The suitability of PA6 and PA6 nanocomposites for such process was assessed by introducing a processing window, defined as the temperature difference between the endset sintering and the onset degradation. In order to explain the heating rate dependence of the processing window, which is particularly relevant in rotational molding, dimensionless analysis was used.

Materials and methods

PA6 matrix was purchased by BASF, under the trade name Ultramid B40. The nanofiller, a montmorillonite modified with 28% by weight of dimethyl benzohydrogenated tallow organic salt (omMMT), was supplied by Laviosa, Italy under the trade name Dellite 43 B.

The thermal stabilizer, a masterbatch of cuprous and potassium halides along with effective lubricants (salts of fatty acid), was supplied by Bruggemann under the name Bruggolen® H 321.

The PA6 mixtures were obtained by melt-compounding in a Haake Polylab with Rheomex PTW 24/40 corotating twin-screw extruder with a screw of 24 mm diameter and length to diameter (*L*/*D*) ratio of 40, using a screw speed of 100 rpm and temperatures of 255, 255, 250, 250, 250, 260, 250, and 260 °C from the hopper to the die section.

Different samples were produced. Sample PA6_H321 is the sample obtained by mixing the PA6 with the thermal stabilizer H321. Sample PA6_43B is the sample obtained by mixing PA6 with the omMMT. Sample PA6_H321_43B is obtained by mixing PA6 with both thermal stabilizer and omMMT. Sample PA6 is the raw material, which was just processed under the similar conditions used for the other samples. The compositions of the tested formulations are reported in Table 1.

X-ray analysis was performed on nanofiller and nanocomposite powders using a Wide angle X-ray Diffractometer, RIGAKU Ultima+ between $2\theta = 1°$ and $2\theta = 10°$.

Rheological analysis was performed at different temperatures, ranging from 503 to 533 K, using a Rheometric Scientific Ares instrument, equipped with a 25-mm cone and plate geometry, varying the shear rate between 0.05 and 1 s^{-1}, using a gap of 0.1 mm.

TMA was performed using a Perkin Elmer TMA 7 equipped with an expansion probe. Materials were pulverized with a Retsch Z100 ultracentrifugal mill, equipped with a 0.5 mm sieve. Powders were placed in an aluminum pan (6 mm diameter) and heated in the TMA apparatus from room temperature to 623 K at different heating rates (5–10–15–20 K min^{-1}), holding a constant pressure (1 mN, corresponding to 35 kPa). During each test, holding a constant force on the sample and increasing the temperature resulted in a decrease of the sample thickness, due to polymer sintering [5]. Accordingly, neglecting the density variation of the polymer due to thermal expansion, the

Table 1 Composition of the tested formulations

Sample	PA6	H321	43B
PA6 (raw matrix)	100	0	0
PA6_43B (PA6 nanocomposite)	96	0	4
PA6_H321 (stabilized PA6)	97	3	0
PA6_H321_43B (stabilized PA6 nanocomposite)	93	3	4

thickness of the sample $\delta(t)$ was related to the bulk density ρ_B by:

$$\rho_B(t,T) = \frac{\text{Mass}}{\text{Volume}} = \frac{\text{Mass}}{A_T\delta(t,T)} \quad (1)$$

where A_T is the surface area of the sample. The rate of sintering was obtained by differentiation of Eq. 1, as:

$$\frac{d\rho_B}{dt}(t,T) = -\frac{\text{Mass}}{A_T\delta^2(t,T)}\frac{d\delta}{dt} \quad (2)$$

Results and discussion

In Fig. 1, the results of X-ray analysis for the nanofiller and the PA6_43B nanocomposite are reported. The diffraction peak of the omMMT, located at $2\theta = 4.6°$, is a measure of lamellar spacing, which can be evaluated to be, according to the Bragg law, $d_L = 1.9$ nm. PA6 nanocomposite does not show any significant diffraction peak correlated to the presence of the nanofiller, which indicates a nanofiller exfoliation or at least a formation of an intercalated structure with $d_L > 7.3$ nm, which is the distance corresponding to $2\theta = 1.2°$.

The rheological behavior of the nanocomposite PA6_43B is reported in Fig. 2, showing a typical non-Newtonian behavior, characterized by a plateau at low shear rate followed by a shear thinning zone. The viscosity of PA6 nanocomposite was fitted by the Cross-Yasuda model [21]:

$$\eta = \frac{\eta_0}{1 + (\lambda\dot{\gamma})^m} \quad (3)$$

where η_0 is the viscosity at zero shear rate, λ is the reciprocal of the shear rate at which the calculated value of η equals $\eta = \frac{\eta_0}{2}$, and the parameter m is related to the power law index, n, as $m = 1–n$. For comparison purposes, in Fig. 2, the Cross-Yasuda model prediction curves are reported. The viscosity curves of sample PA6 also showed

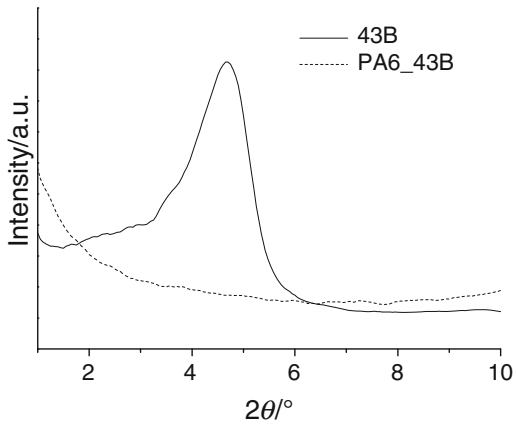

Fig. 1 X-ray diffraction patterns of omMMT and PA6_43B

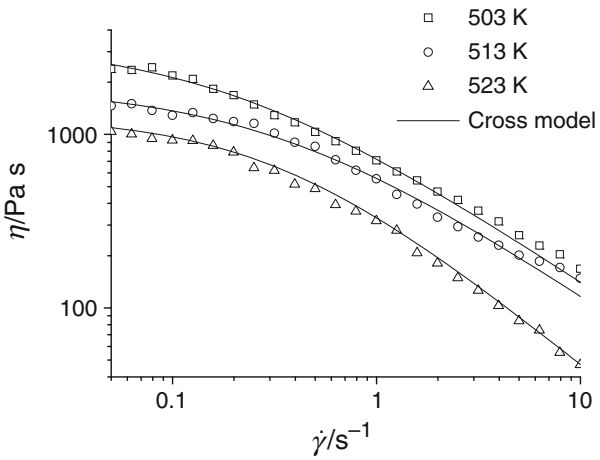

Fig. 2 Viscosity curves for sample PA6_43B at different temperatures and cross model fitting

the typical low share rate plateau, which allowed for fitting of the experimental curves according to the Cross-Yasuda model.

The viscosity curves of sample PA6_H321_43B, reported in Fig. 3, are significantly different from those observed for sample PA6_43B and PA6, being characterized by the absence of the characteristic Newtonian plateau at low shear rate, accounted in the Cross model. In this case, the simpler power law behavior is observed [21]:

$$\eta = \eta_A\dot{\gamma}^{n-1} \quad (4)$$

where η_A is the viscosity corresponding to a shear rate equal to 1 s^{-1} and n is the viscosity number. The power law model prediction is also reported in Fig. 3. Finally, the sample PA6_H321 showed a typical Newtonian behavior.

The most relevant property governing the viscous forces during the sintering process is the "zero shear rate" viscosity, η_0. For samples PA6 and PA6_43B, which showed a low shear rate plateau, the zero shear rate viscosity coincides with the η_0 reported in Eq. 3. For sample PA6_H321_43B, showing the power law behavior, η_0 was taken at $\dot{\gamma} = 0.05\,s^{-1}$, which is the initial shear rate value used in the reported measurements. Finally, for sample PA6_H321, showing a Newtonian behavior, the zero shear rate viscosity was taken as the average value of the viscosity measured in the range between 0.05 and 1 s^{-1}.

The values of η_0 determined for each sample at the three temperatures, reported in Table 2, were fitted according to a modified Arrhenius equation, also known as Vogel–Tammann–Fulcher (VTF) equation [22, 23]:

$$\eta_0 = K_0\exp\left(\frac{E_v}{R(T - T_0)}\right) \quad (5)$$

In which, K_0 is a pre-exponential factor, E_v is the activation energy, R is the universal gas constant, and T_0 is a

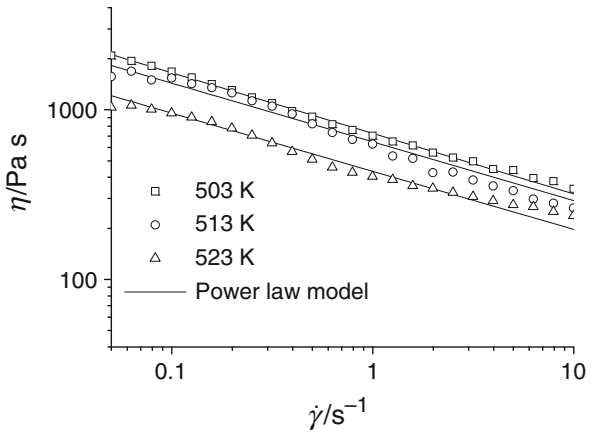

Fig. 3 Viscosity curves for sample PA6_H321_43B at different temperatures and power law model fitting

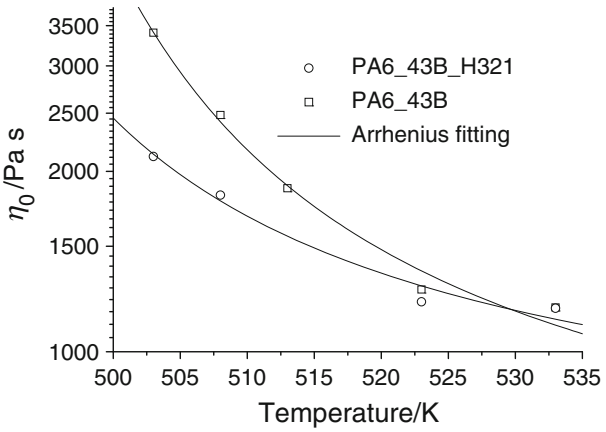

Fig. 4 Zero shear rate viscosity for PA_43B PA6_43B_H321 and Arrhenius fitting

characteristic temperature, in correspondence of which the viscosity diverge. The introduction of T_0 accounts for the fact that, in the solid state, the viscosity of the materials can be considered infinite. The fitting parameters of experimental η_0 viscosities according to Eq. 5 for the four samples are reported in Table 2. A comparison between Eq. 5 prediction and experimental data is shown in Fig. 4 for samples PA6_43B and PA6_43B_H321. The zero shear rate viscosities extrapolated at 503 K are also reported in Table 2. The data reported in Table 2 show that the addition of the thermal stabilizer to PA6 is responsible for a significant decrease of viscosity. The similar behavior is observed when the thermal stabilizer is added to the nanofilled PA6. This is attributed to the effect of the masterbatch, added together with the stabilizer, which is mainly composed of lubricants. On the other hand, the addition of the nanofiller causes an increase of viscosity. These counteracting factors are responsible for a viscosity of the sample PA6_43B about twice the viscosity of PA6, whereas sample PA6_43B_H321 has a viscosity comparable to that of neat PA6. The zero shear rate viscosity was also fitted by a pure Arrhenius expression (obtained by Eq. 5) by setting $T_0 = 0$ K), and the results obtained for the activation energy (labeled as E_v') are also reported in Table 2.

Table 2 Arrhenius fit results for zero shear rate viscosity

	K_0/ Pa s	E_v/R/ K	T_0/ K	η_0 (503 K)/ Pa s	E_v'/R/ K
PA6	163	56	479	1,680	39,758
PA6_43B	434	52	478	3,470	11,552
PA6_H321	7.5	138	472	640	22,870
PA6_43B_H321	590	39	472	2,060	7,650

K_0 Pre-exponential factor in VTF equation, E_v/R activation energy in VTF equation, T_0 temperature at which viscosity diverges, η_0 zero shear rate extrapolated at 503 K according to VTF model, E_v'/R activation energy in Arrhenius equation

The evolution of bulk density as a function of temperature obtained from TMA analysis for sample PA6 during heating at 20 K min^{-1} is reported in Fig. 5. Below melting temperature, density increase is negligible, since powder sintering of semicrystalline polymers can only occur in the molten phase. Above melting temperature, the density increases due to powder coalescence and void removal, which are the two mechanisms involved in polymer sintering. Powder coalescence occurs at lower temperatures, whereas the void removal stage is observed at higher temperatures. The rate of sintering curve obtained according to Eq. 2, and reported in Fig. 5, shows a distinct peak in correspondence of the powder coalescence step. The peak associated to further densification due to voids removal is much smaller and visible in the inset of Fig. 5 between 540 and 587 K. Finally, increasing the temperature, a significant density reduction is observed as a consequence of gas formation deriving from polymer degradation.

The characteristic values of the onset ($T_{s,onset}$) and endset ($T_{s,endset}$) temperature of sintering, the temperature corresponding to the main peak of the derivative curve ($T_{s,peak}$), the onset temperature of degradation ($T_{d,onset}$), and the maximum value of density are reported in Table 3 for the tested heating rates. DSC analysis performed on PA6 sample was used to calculate an onset degradation temperature of 534 K, which is approximately the value of 532 K reported in Table 3, and confirms the presence of degradation phenomena which involve a density decrease of the material.

In view of a potential application in rotational molding, the polymer should be able to attain complete sintering before its degradation begins. Referring to the characteristic data reported in Table 3, it is therefore possible to introduce a processing window, which is defined as the

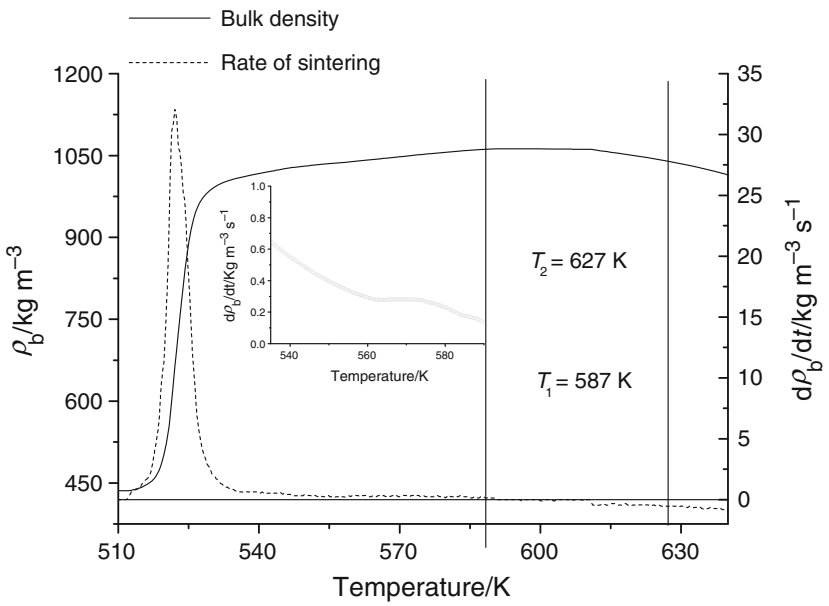

Fig. 5 Experimental bulk density and rate of sintering for PA6 at 20 K min^{-1}

difference between the onset degradation and the endset sintering:

$$\Delta T_{\text{processing}} = T_{\text{d,onset}} - T_{\text{s,endset}} \quad (6)$$

Full sintering in a TMA test can be easily attained even if the processing window is small, since in a 1-mm thick sample the temperature gradients across the sample thickness can be neglected. On the other hand, during rotational molding, higher thicknesses (3–6 mm) and non-uniform heating are responsible temperature gradients across the thickness that can attain 40 K [24]. This implies that when the sintering of the "cold" side of the polymer, i.e., the inner surface of rotational molded component, takes place, the "hot" side of the material, in contact with the mold wall, must not degrade. Therefore, rotational molding becomes possible only if the processing window is wider than the maximum temperature gradient across sample thickness. Assuming a maximum temperature gradient of 40 K, according to former studies [24], a polymer is suitable for rotational molding when:

$$\Delta T_{\text{processing}} > 40\,\text{K} \quad (7)$$

The TMA results indicate that neat PA6 is not suitable for the rotational molding process because, as shown in Table 3, the temperature difference between the endset sintering and the onset degradation is always lower than 40 K for every heating rate.

As shown in Table 3, another relevant factor influencing the width of the processing window is the heating rate. As reported in Fig. 6 for PA6, increasing the heating rate the powder coalescence shows a relatively weak dependence on the heating rate (there is a difference of about 18 K between the maximum rate sintering calculated at 5 and 20 K min^{-1}), whereas the void removal stage shows a very strong dependence from the heating rate (there is a difference of about 76 K between the endset temperature of sintering calculated at 5 and 20 K min^{-1}). The reason for the different temperature dependence of the two phenomena can be ascribed to the fact that powder coalescence is mainly governed by the viscosity of the material [3, 4] whereas void removal is mainly governed by gas diffusivity inside the matrix [9]. Furthermore, the void removal stage is more evident as the heating rate increases, whereas it is overlapped with the coalescence stage at the lower scanning rates. In any case, an increase of the scanning rate yields to a widening of the processing window, always lower than 40 K for PA6.

Addition of the nanofiller does not involve a significant modification of the sintering characteristic of the polymer, as confirmed by TMA curve of PA6_43B, reported in Fig. 7. The onset sintering temperature and the peak temperature, also reported in Table 3, are not significantly modified compared to neat PA6. On the other hand, the presence of the nanofiller involves a significant decrease of the onset degradation temperature of the polymer, as evidenced by the data reported in Table 3 and Fig. 7. This is due to the presence of the organic modifier of the nanofiller, which is characterized by a very poor thermal stability [25], thus enhancing the degradation rate of the polymer. As a consequence of the accelerated kinetics of degradation, the maximum density attained by the material during sintering is much lower for sample PA6_43B compared to neat PA6, as reported in Fig. 7 and Table 3, which indicates that PA6_43B is not suitable for rotational molding.

The effect of the addition of a thermal stabilizer is shown Fig. 8, where sintering curves of sample PA6_H321

Table 3 Characteristic parameters of the sintering process

Sample	Heating rate/K min^{-1}	$T_{s,onset}$/K	$T_{s,peak}$/K	$T_{s,endset}$/K	$T_{d,onset}$/K	ρ_{max}/kg m^{-3}
PA6	5	502	504	513	530	1,158
	10	506	510	521	532	1,111
	15	516	519	554	580	1,104
	20	519	522	588	590	1,062
PA6_43B	5	497	501	–	504	867
	10	504	508	–	511	1,082
	15	510	513	–	517	944
	20	514	518	–	522	1,011
PA6_H321	5	498	501	506	571	1,100
	10	500	503	510	587	1,149
	15	512	515	522	600	1,135
	20	513	517	525	618	1,034
PA6_H321_43B	5	497	501	542	601	1,170
	10	501	504	569	600	1,280
	15	512	515	590	623	1,130
	20	514	518	586	622	1,060

are reported, and in Table 3, where the characteristic temperatures of sintering and degradation are listed. PA6_H321 powder shows a degradation onset about 40 K higher than that of neat PA6. In addition, the void removal stage of PA6_H321 is much faster compared to sample PA6, therefore leading to a significant decrease of the endset sintering temperature. As a consequence of the accelerated void removal, and of the delayed degradation, the sample PA6_H321 shows a wider processing window that can extend to 90 K. Even in this case, as reported in Table 3, the processing window increases as the heating rate increases as well. Therefore, PA6_H321 can be considered as a candidate material for rotational molding, since the processing window is always wider than the maximum temperature gradients characterizing typical processing conditions in rotational molding.

Finally, the TMA results for sample PA6_H321_43B are reported in Fig. 9. Compared to sample PA6_H321, the addition of the nanofiller does not involve any significant modification of the initial stage of sintering. On the other hand, the void removal stage is much slower for sample PA6_H321_43B compared to sample PA6_H321. This is in agreement with the fact that the void removal stage is governed by the gas diffusivity in the polymer matrix, and it is well known that addition of nanofillers can cause a drastic gas decrease and vapor diffusivity [26, 27]. In contrast with what observed by comparing samples PA6 with PA6_43B, the addition of the nanofiller involves an

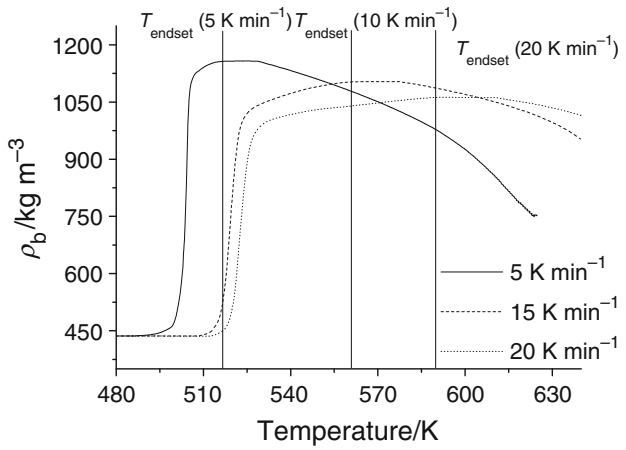

Fig. 6 TMA curves for sample PA6 at different heating rates

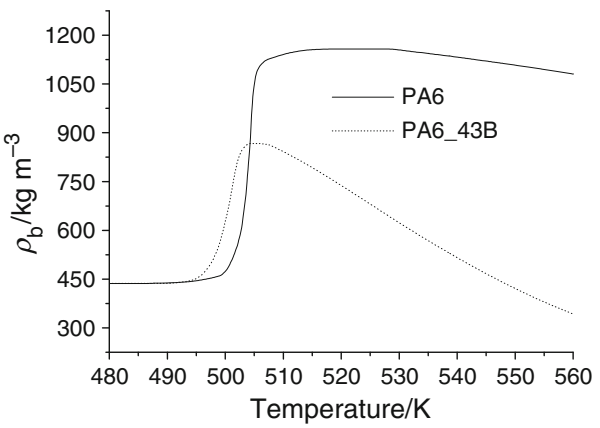

Fig. 7 Experimental bulk density for PA6 and PA6_43B at 5 K min^{-1}

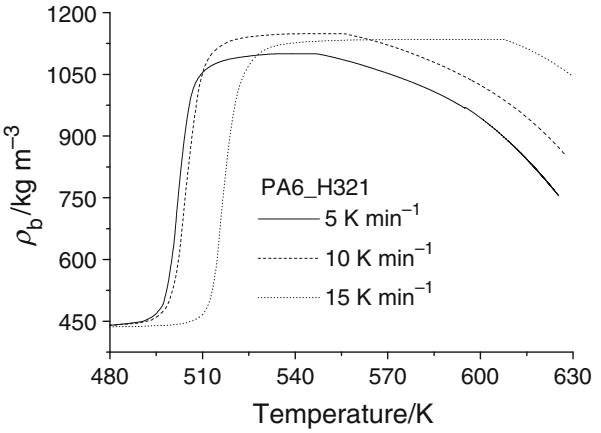

Fig. 8 Experimental bulk density for PA6_H321 at different heating rates

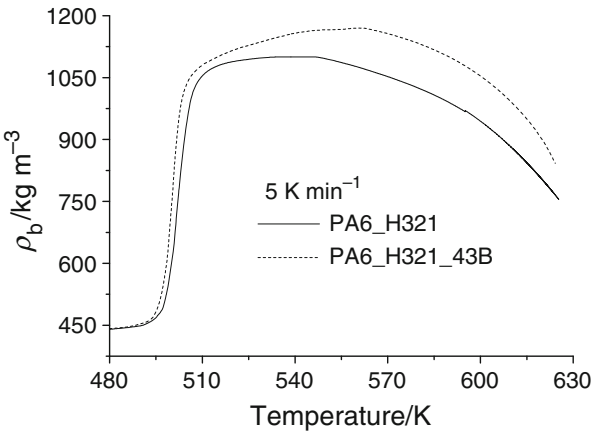

Fig. 9 Experimental bulk density for PA6_H321 and PA6_H321_43B at 5 K min^{-1}

increase of the thermal stability of the polymer. As shown in Table 3, the processing window for sample PA6_H321_43B ranges between 60 and 40 K, with the wider processing window encountered at the lower heating rates, indicating the suitability of PA6_H321_43B to rotational molding.

Dimensionless analysis of sintering

In the previous section, it was shown that the density evolution of the material during the TMA measurement is determined by three different phenomena:

a) Powder coalescence, dominated by the viscosity of the material;
b) Void removal, dominated by the air diffusivity through the molten polymer;
c) Degradation, depending on the thermo-oxidative behavior of the material.

The relevance of each of these mechanisms in different ranges of temperatures can be studied by introducing proper dimensionless numbers.

The powder coalescence can be studied introducing the dimensionless number G_1 [20]:

$$G_1 = \frac{\Gamma \Delta T_{\text{coalescence}}}{\beta a_0 \eta_0} \tag{8}$$

where $\Gamma = 0.035$ N m^{-1} is the surface tension of the polymer [28], $a_o = 500$ μm is the average diameter of powders, $\Delta T_{\text{coalescence}}$ is the temperature interval of powder coalescence, and β is the scanning rate. G_1 represents the ratio between surface tension forces, Γ/a_0, and viscous forces, $\eta_0\beta/\Delta T_{\text{colaescence}}$ or equivalently the ratio between the characteristic time of the experiment $\Delta T_{\text{coalescence}}/\beta$ and the characteristic time of the coalescence process, $\eta_0 a_0/\Gamma$. G_1 for neat PA6 was calculated in correspondence of the peak temperature of coalescence (reported in Table 3) at different heating rates, using the $\Delta T_{\text{coalescence}}$ and η_0 values reported in Table 4. The values of η_0 reported in Table 4 were obtained according to Eq. 5, using the Arrhenius fitting parameters reported in Table 2. G_1 for neat PA6 ranges between 5.4 and 8. Similar calculations were performed for all the other samples, obtaining the G_1 values ranging between 2.5 and 6. In each case, the calculated values of G_1 are higher than unity, indicating that powder coalescence takes place when the surface tension forces, promoting coalescence, become much higher than viscous forces, opposing to powder coalescence.

Following a similar approach it is possible to study the void removal stage, occurring as a consequence of diffusion. Dimensionless analysis of the Fick's law leads to the introduction of the dimensionless number G_2:

$$G_2 = \frac{D\Delta T_{\text{bubblerem}}}{\beta L^2} \tag{9}$$

In which, D is the diffusivity of the gas (air) in PA6, L is the diffusion length (assumed to be equal to half the thickness of samples), $\Delta T_{\text{bubblerem}}$ is the temperature interval for void removal (about 40 K for all samples), and β is the heating rate. The dimensionless number G_2 represents the ratio between the characteristic time of the experiment, $\Delta T_{\text{bubblerem}}/\beta$, and the characteristic time for

Table 4 Data used for the calculation of coalescence dimensionless number for PA6

Rate/K min^{-1}	$\Delta T_{\text{sintering}}$/K	η_0 ($T_{\text{peak,sintering}}$)/Pa s	G_1
5	9	1,545	4.9
10	10	1,003	4.2
15	14	668	5.9
20	18	606	6.3

diffusion (L^2/D). The characteristic time for bubble diffusion is inversely proportional to the diffusivity of the gas, as already found by Gogos [9].

An Arrhenius-like dependence of diffusivity from temperature was assumed, and the Arrhenius parameters were collected from Ref. [29]:

$$D = D_0 \exp\left(-E_D/RT\right) \tag{10}$$

$$\frac{E_D}{R} = \left[6400 - 0.16\left(T_g - 298\right)^2\right] \tag{11}$$

$$\log_{10} D_0 = 0.001\frac{E_D}{R} - 9.8 \tag{12}$$

Using a value of $T_g = 322$ K for neat PA6, determined from DSC analysis, $E_D/R = 6322$ K and $D_0 = 3.3\ \mathrm{E}^{-4}\ \mathrm{m}^2\ \mathrm{s}^{-1}$ were calculated from Eqs. 11 and 12, respectively. $D = 1.8\ \mathrm{E}^{-9}\ \mathrm{m}^2\ \mathrm{s}^{-1}$ and $D = 5.6\ \mathrm{E}^{-9}\ \mathrm{m}^2\ \mathrm{s}^{-1}$ were obtained from Eq. 10 at the temperatures corresponding to the first (powder coalescence) and second (void removal) peak of $\mathrm{d}\rho_B/\mathrm{d}t$, i.e., 522 and 570 K at 20 K min^{-1}, respectively. The corresponding values of G_2 are 0.8 and 2.7. A value of $G_2 = 0.8$ at 522 K indicates that in correspondence of the coalescence step the diffusion time is higher than the characteristic time of the experiment, so limiting an efficient void removal. In contrast, a value of $G_2 = 2.7$ at 570 K indicates that void removal can occur at this temperature due to the reduction of the diffusion time, now much lower than the characteristic time of the experiment. Heating at 5 K min^{-1}, the characteristic time of the experiments increases leading to $G_2 = 2.3$ in correspondence of the peak temperature of coalescence ($T = 504$ K, $D = 1.2\ \mathrm{E}^{-9}\ \mathrm{m}^2\ \mathrm{s}^{-1}$), indicating that in this case significant void removal can occur also during the powder coalescence step. This also explains why the void removal step is clearly observed when tests are performed at higher heating rates, whereas it overlaps with the coalescence steps when tests are performed at lower heating rates.

Analysis of the degradation

The degradation rate can be expressed as a function of temperature and degree of degradation, α, as:

$$\frac{\mathrm{d}\alpha}{\mathrm{d}t} = k_{to}\exp\left(-\frac{E_{to}}{\mathrm{RT}}\right)f(\alpha) \tag{13}$$

In which, k_{to} and E_{to} are the kinetic constant and activation energy of the degradation process, respectively, and $f(\alpha)$ is a generic function of the degree of degradation [20]. The bulk density can be expressed as a function of the degree of degradation:

$$\rho_b = \rho_{max}(1 - \alpha) \tag{14}$$

which by inversion and differentiation becomes:

$$\frac{\mathrm{d}\alpha}{\mathrm{d}t} = -\frac{1}{\rho_{max}}\frac{\mathrm{d}\rho_b}{\mathrm{d}t} \tag{15}$$

which by substitution into Eq. 13 yields:

$$\frac{\mathrm{d}\rho_b}{\mathrm{d}t} = -k_{to}\rho_{max}\exp\left(-\frac{E_{to}}{\mathrm{RT}}\right)f\left(1 - \frac{\rho_b}{\rho_{max}}\right) \tag{16}$$

Finally, by taking the natural logarithms on both sides of Eq. 16:

$$\ln\left(-\frac{\mathrm{d}\rho_b}{\mathrm{d}t}\right) = \ln(k_{to}\rho_{max}) + \ln\left[f\left(1 - \frac{\rho_b}{\rho_{max}}\right)\right] - \frac{E_{to}}{\mathrm{RT}} \tag{17}$$

Therefore, by plotting $\ln(\mathrm{d}\rho_b/\mathrm{d}t)$ as a function of $1/T$ at constant values of ρ_b (which is known as Friedman plot), for the tests performed at different heating rates, the activation energy for degradation can be determined by linear fitting according to Eq. 17. In particular, by considering only the initial stages of degradation, the ratio $\frac{\rho_b}{\rho_{max}}$ is almost unity, and therefore the term $\ln\left[f\left(1 - \frac{\rho_b}{\rho_{max}}\right)\right]$ can be approximated as $\ln[f(0)]$, which is independent on the heating rate. An example of the Friedman plot is reported in Fig. 10. The plots at different values of densities all lie on the same curve, and therefore they can be linearly fitted simultaneously.

In Fig. 11, the activation energies of degradation determined by the Friedman plots for the four samples are reported. As it can be observed, the activation energy for degradation is, except for sample PA6_43B_H321, lower than the activation energy for viscous flow reported in Table 2.

On the other hand, the difference in the activation energy for samples PA6 and PA6_43B is lower than the error bars, which allow to conclude that the activation energy of the two materials is roughly similar. On the contrary, the addition of thermal stabilizer causes an effective increase of the activation energy for degradation.

The different activation energies of the three processes occurring during the heating of the powders can explain the different behavior observed at the different heating rates. In order to explain the heating rate dependence of the bulk density curves, it must be considered that a process which is characterized by the higher activation energy shows a weaker dependence on the heating rate.

Therefore, the powder coalescence step, which is the one characterized by the higher activation energy (the one calculated for the viscosity and reported in Table 2), shows the weaker dependence on the heating rate.

For the sample PA6, the activation energy for degradation (4639 K) is lower than the activation energy for diffusion (6320 K). Therefore, the degradation step is more sensitive to the heating rate than the diffusion step.

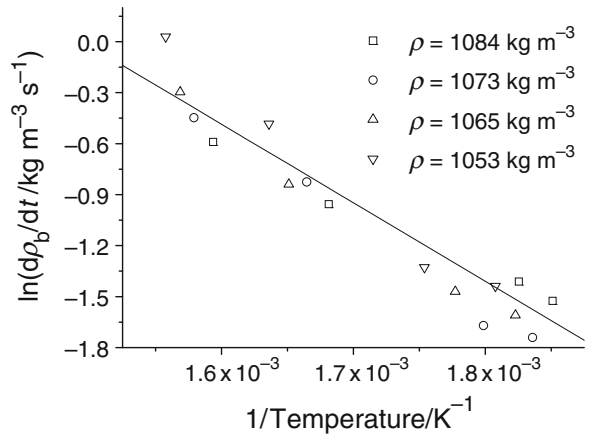

Fig. 10 Friedman plot for the degradation of PA6

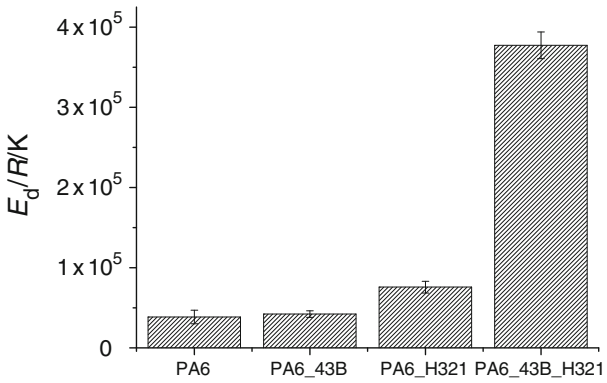

Fig. 11 Activation energies for degradation of PA6 and its nanocomposites

Increasing the heating rate, both processes are shifted at higher temperatures, but the shift is more consistent for the degradation process. This involves an increase of the processing window, which is in agreement with the data reported in Table 3. On the other hand, the sample PA6_43B_H321 has an activation energy of degradation much higher than that of diffusion. Therefore, increasing the heating rates yields a decrease of the width of the processing window, as evidenced by the results reported in Table 2.

Conclusions

In this study, TMA analysis has been used for on-line monitoring of the bulk density evolution of PA6 and PA6 nanocomposites powders during thermal treatment. Results obtained from TMA analysis indicate that the sintering of PA6 and PA6 nanocomposite takes place above the melting temperature of the polymer, and consists in two different steps, namely powder coalescence and void removal. The main issue in the sintering of PA6 and PA6 nanocomposites is related to the presence of relevant degradation phenomena, which occur at quite low temperatures, and involve the formation of a gaseous phase in the molten polymer, which is responsible of a decrease of the density. In view of potential industrial application, it is therefore possible to define a processing window, which is defined as the difference between the endset sintering and the onset degradation. PA6 and PA6 nanocomposite made with omMMT show very narrow processing window, thus resulting not suitable for sintering-based processes. The addition of thermal stabilizer involves a significant delay of the degradation of the material, which involves a broadening of the processing window at very high value (about 80 K), making stabilized PA6 a candidate materials for sintering-based processes.

The existence of the three steps, and their dependence on the heating rate, has been studied by means of dimensionless analysis. It was shown that the powder coalescence step mainly depends on the evolution of the material viscosity, and therefore it can take place when the viscous forces become sufficiently lower than surface tension forces. On the other hand, the void removal step depends on the gas diffusivity in the molten matrix, and it takes place only when the characteristic time of diffusion becomes much lower than the characteristic time of experiment. The different heating rate sensitivity of the two stages has been explained by considering the different activation energies of viscosity and diffusivity. Finally, the activation energy of degradation has been determined by Friedman plots. The width of the processing window has been correlated to the heating rate by considering the different activation energies of diffusion and degradation.

Acknowledgements Authors wish to thank the "Regione Puglia" for financial support of the project "INCOR—Innovative thermoplastic matrix composites for rotational moulding".

References

1. Kandis M, Bergman TL. Observation, prediction, and correlation of geometric shape evolution induced by non-isothermal sintering of polymer powder. J Heat Transf-Trans ASME. 1997;119:824–31.
2. Liu SJ. International polymer processing XIII. Munich: Hanser Publishers; 1998.
3. Bellehumeur CT, Bisaria MK, Vlachopoulos J. An experimental study and model assessment of polymer sintering. Polym Eng Sci. 1996;36:2198–207.
4. Kontopoulou M, Vlachopoulos J. Bubble dissolution in molten polymers and its role in rotational molding. Polym Eng Sci. 1999;39:1189–98.
5. Greco A, Maffezzoli A. Polymer melting and polymer powder sintering by thermal analysis. J Therm Anal Calorim. 2003;72:1167–74.
6. Greco A, Maffezzoli A. Powder-shape analysis and sintering behavior of high-density polyethylene powders for rotational molding. J Appl Polym Sci. 2004;92:449–60.

7. Bellehumeur CT, Kontopulou M, Vlachopoulos J. The role of viscoelasticity in polymer sintering. Rheol Acta. 1998;37:270–8.
8. Kontopoulou M, Vlachopoulos J. Melting and densification of thermoplastic powders. Polym Eng Sci. 2001;41:155–69.
9. Gogos G. Bubble removal in rotational molding. Polym Eng Sci. 2004;44:388–94.
10. Rezaei M, Ebrahimi NG, Kontopoulou M. Thermal properties, rheology and sintering of ultra high molecular weight polyethylene and its composites with polyethylene terephthalate. Polym Eng Sci. 2005;45:678–86.
11. Drummer D, Rietzel D, Kuhnlein F. Development of a characterization approach for the sintering behavior of new thermoplastics for selective laser sintering. Phys Procedia. 2010;5:533–42.
12. Kim J, Creasy TS. Selective laser sintering characteristics of nylon 6/clay-reinforced nanocomposite. Polym Test. 2004;23:629–36.
13. Chung H, Das S. Functionally graded nylon-11/silica nanocomposites produced by selective laser sintering. Mater Sci Eng. 2008;487:251–7.
14. Salmoria GV, Leite JL, Paggi RA. The microstructural characterization of PA6/PA12 blend specimens fabricated by selective laser sintering. Polym Test. 2009;28:746–51.
15. Dong L, Makradi A, Ahzi S, Remond Y, Sun X. Simulation of the densification of semicrystalline polymer powders during the selective laser sintering process: application to nylon 12. Polym Sci Ser A. 2008;50:704–9.
16. Asgarpour M, Bakir F, Khelladi S, Khavandi A, Tcharkhtchi A. Characterization and modeling of sintering of polymer particles. J Appl Polym Sci. 2001;119:2784–92.
17. Jain PK, Pandey PM, Rao PVM. Selective laser sintering of clay-reinforced polyamide. Polym Compos. 2010;31:732–43.
18. Oliveira MJ, Cramez MC, Garcia CB, Kearns MP, Maziers E. Effect of the processing conditions on the microstructure and properties of rotational molded polyamide 11. J Appl Polym Sci. 2008;108:939–46.
19. Opfermann J, Blumm J, Emmerich WD. Simulation of the sintering behavior of a ceramic green body using advanced thermokinetic analysis. Thermochim Acta. 1998;318:213–20.
20. Greco A, Strafella A, La Tegola C, Maffezzoli A. Assessment of the relevance of sintering in thermoplastic commingled yarn consolidation. Polym Compos. 2011;32(4):657–64.
21. Dealy JM, Larson RG. Structure and rheology of molten polymers. Munich: Carl Hanser Verlag; 2006.
22. Ojovan MI, Lee WE. Fragility of oxide melts as a thermodynamic parameter. Phys Chem Glasses. 2005;46(1):7–11.
23. Vogel H. The law of temperature dependence of the viscosity of fluids. Phys Z. 1921;22:65.
24. Greco A, Maffezzoli A, Vlachopoulos J. Simulation of heat transfer during rotational molding. Adv Polym Tech. 2003;22:271–9.
25. Shah RK, Paul DR. Organoclay degradation in melt processed polyethylene nanocomposites. Polymer. 2006;47:4075–84.
26. Esposito Corcione C, Cavallo A, Pesce E, Greco A, Maffezzoli A. Evaluation of the degree of dispersion of nanofillers by mechanical, rheological, and permeability analysis. Polym Eng Sci. 2011;51:1280–5.
27. Esposito Corcione C, Mensitieri G, Maffezzoli A. Analysis of the structure and mass transport properties of nanocomposite polyurethane. Polym Eng Sci. 2009;49:1708–18.
28. Son Y. Measurement of interfacial tension between polyamide-6 and poly(styrene-co-acrylonitrile) by breaking thread method. Polymer. 2001;42:1287–91.
29. Van Krevelen DW, te Nijenhuis K. Properties of polymers. 4th ed. Amsterdam: Elsevier; 2009.